Journal of Membrane Science 713 (2025) 123276

Contents lists available at ScienceDirect

Journal of Membrane Science

journal homepage: www.elsevier.com/locate/memsci

Development of a local wall concentration model for the design of single pass tangential flow filtration (SPTFF) systems with viral vector surrogates

Akshay S. Chaubal, Alexis J. Single, Andrew L. Zydney [*]

Department of Chemical Engineering, The Pennsylvania State University, University Park, PA, 16802, USA

ARTICLE INFO

Keywords:
Ultrafiltration
SPTFF
Critical flux
Viral vectors
AAV
Lentivirus

ABSTRACT

Recent advances in the use of viral vectors for gene therapy has created a need for efficient downstream processing of these novel therapeutics. Single-pass tangential flow filtration (SPTFF) can potentially improve final product quality via reductions in shear, and it can increase manufacturing productivity via simple implementation into continuous/intensified processes. This study investigated the impact of variations in pressure and flow rate along the length of the membrane on overall SPTFF performance. Constant-flux filtration experiments at feed fluxes from 14 to 420 L/m^2/h (Reynolds numbers <20) were performed using Pellicon® 3 TFF cassettes with fluorescent nanoparticles as model viral vectors. The location of nanoparticle accumulation shifted towards the filter outlet at high conversion and was also a function of the permeate flow configuration. These phenomena were explained using a newly developed concentration polarization model that predicts the distribution in local wall concentration over the length of the membrane. The model accurately captured the observed nanoparticle accumulation trends, including the effects of the permeate flow profile (co-current, divergent, or convergent flow) on nanoparticle accumulation within the SPTFF module. Nanoparticle accumulation at moderate conversion was more uniform using convergent flow, but nanoparticle accumulation at 80 % conversion (5x concentration factor) can be minimized using a divergent flow configuration. The local wall concentration model was also used to evaluate the critical flux by assuming that fouling occurs when the nanoparticle concentration at any point along the membrane surface exceeds 15 % by volume. These results provide important insights for the design and operation of SPTFF technology for inline concentration of viral vectors.

1. Introduction

Viral vectors have emerged as leading candidates for the delivery of both mRNA and DNA for gene therapy applications [1]. To date, 19 viral vector products have been approved by the FDA, with lentiviral vectors (LVs) and adeno-associated viral vectors (AAVs) collectively accounting for nearly 75 % of these approvals [2]. *Atidarsagene autotemcel* was recently approved in the U.S. as the first and only treatment for early-onset metachromatic leukodystrophy, in which hematopoietic stem cells are transduced with LVs containing the human arylsulfatase A gene [3]. Additionally, *fidanacogene elaparvovec-dzkt* – which utilizes AAVs to deliver the gene for expression of Factor IX – was approved in April 2024 as a one-time treatment for adults with hemophilia B [4].

Viral vectors are produced in mammalian cells, with downstream purification typically involving clarification of the cell culture fluid, ultrafiltration using a relatively open pore size membrane to concentrate the dilute vector and reduce the concentration of host cell proteins, one or more chromatography step(s) to remove product-related impurities (including empty capsids), and an ultrafiltration/diafiltration step (UF/DF) for product formulation [5,6]. Several studies have examined the performance of tangential flow filtration (TFF) for batch concentration of viral vectors, with the feed recirculated through the membrane module to obtain the desired degree of concentration. The pumping and high shear rates employed in typical TFF modules can cause virus degradation [7] and protein aggregation [8,9], both of which may be of concern in the processing of viral vectors. Previous studies with LVs [5,10] and AAVs [11] report TFF process yields ranging from 16 % to nearly 100 % [5].

Single-pass tangential flow filtration (SPTFF) – in which the required concentration factor is attained in a single pass through the membrane module – is of growing interest as an alternative to traditional TFF [12]. The elimination of the recycle loop can improve product quality (by reducing exposure to shear and pumping) and increase overall

---

[*] Corresponding author. Department of Chemical Engineering, 404 Chemical & Biomedical Engineering Building, The Pennsylvania State University, University Park, PA, 16802, USA.

E-mail address: zydney@engr.psu.edu (A.L. Zydney).

https://doi.org/10.1016/j.memsci.2024.123276
Received 10 July 2024; Received in revised form 23 August 2024; Accepted 31 August 2024

Nomenclature

Abbreviations

LV	Lentiviral vectors
AAV	Adeno-associated viral vectors
NP	Nanoparticles
TFF	Tangential flow filtration
SPTFF	Single pass tangential flow filtration
TMP	Transmembrane pressure
LMH	Liters per m^2 per hour
MWCO	membrane nominal molecular weight cutoff

Symbols

C_b	local bulk nanoparticle concentration [particles m^{-3}]
C_w^{max}	maximum wall concentration along membrane surface [particles m^{-3}]
C_w	local wall concentration [particles m^{-3}]
d_h	channel hydraulic diameter [m]
D	nanoparticle diffusion coefficient [m^2 s]
f_p	fraction of permeate collected from port “P1” [−]
h	height of the retentate channel [m]
J	local permeate flux [m s^{-1}]
J_{bl}	boundary layer critical flux [m s^{-1}]
J_{feed}	feed flux [m s^{-1}]
J_{foul}	critical flux for fouling [m s^{-1}]
k_o	local mass transfer coefficient [m s^{-1}]
l_m	spacer mesh length [m]
L	channel length [m]
L_p	membrane permeability [m Pa^{-1} s^{-1}]
m_{bl}	number of nanoparticles within the boundary layer [−]
P_p	local pressure in the permeate channels [Pa]
P_r	local pressure in the retentate channel [Pa]
Q_p	local flow rate in the permeate channel [m^3 s^{-1}]
Q_r	local flow rate in the retentate channel [m^3 s^{-1}]
Re	Reynolds number [−]
Sc	Schmidt number [−]
Sh	Sherwood number [−]
U	local crossflow velocity [m s^{-1}]
w	channel width [m]
z	cartesian coordinate [m]

Greek symbols

β_p	permeate pressure loss parameter [m^{-4}]
β_r	retentate pressure loss parameter [m^{-4}]
δ	concentration boundary layer thickness [m]
μ	inlet suspension viscosity [Pa s]
ν	suspension viscosity [m^2 s^{-1}]
φ	overall permeate conversion [%]

manufacturing productivity (through the development of continuous or interconnected processes) [13,14]. A number of studies have demonstrated the use of SPTFF for inline concentration of monoclonal antibodies, either for elimination of tankage constraints [15] or to increase the productivity of the subsequent affinity chromatography step [16]. Tona et al. [17] suggested that SPTFF could be used for process intensification in the production of LV vectors, but no actual data were provided. Chaubal and Zydney [18] showed that SPTFF could provide stable inline concentration of 100 nm nanoparticles, which were used as a model system for LV.

A number of investigators have developed models for SPTFF performance, focusing on the behavior of monoclonal antibodies (mAbs). Huter et al. [19] and Thakur et al. [20] developed models in which the filtrate flux is limited by the resistance of the membrane and mass transfer boundary layer using a resistance-in-series approach, but the boundary layer resistance had to be evaluated by fitting the model to the experimental data obtained with monoclonal antibodies. Krippl et al. used an artificial neural network to predict SPTFF performance, but it is unclear whether this approach can be readily extended to viral vectors [21]. Jabra et al. developed a more mechanistic model in which the flux was limited by protein concentration polarization effects, with SPTFF performance thereby limited by the high viscosity of the concentrated mAb solution [22,23]. This approach is unlikely to be valid for dilute suspensions of AAV or LV in which the viscosity remains relatively constant. Chaubal and Zydney [18] used a concentration polarization model to describe the critical flux in SPTFF, but they neglected the variation in retentate flow rate and nanoparticle concentration over the length of the SPTFF module. Thus, their analysis is strictly limited to relatively low concentration factors.

The objective of the current work was to develop a more complete modeling framework for the analysis and design of SPTFF processes for LV and AAV that explicitly accounts for the variation in local concentration, pressure, and flow rate in both the retentate and permeate channels within the SPTFF module. The resulting model was used to predict the local wall concentration, and thus the location of particle accumulation, as a function of operating conditions and flow configuration. The model predictions were validated using experimental data obtained with 100 nm and 20 nm carboxylate-modified fluorescent nanoparticles as model systems for LV and AAV, respectively. Note that a number of prior studies have similarly used polymeric nanoparticles as surrogates for an array of virus-based therapeutics, including rhabdovirus [24], live-attenuated virus vaccines [25], AAV [26,27], and adenovirus [28]. The results presented in this study provide a foundation for model-based optimization of SPTFF for dilute nanoparticle suspensions such as those encountered in the production of important viral vectors for gene therapy applications.

2. Materials and methods

2.1. Nanoparticles

Experiments were performed using 100 and 20 nm Fluospheres®, fluorescently-labeled carboxylate-modified polystyrene latex nanoparticles (ThermoFisher Scientific, Waltham, United States). These nanoparticles were specifically selected given their similar size and charge to lentivirus and adeno-associated virus, with the size and zeta potential evaluated via dynamic light scattering (DLS) using a Zetasizer Nano ZS (Malvern Panalytical, Malvern, United Kingdom). Buffer conditions for DLS along with size and zeta potential measurements are presented in Table S1. In addition, the concentration of the Fluospheres® were readily evaluated by fluorescence intensity using a Tecan® Infinite m200 Pro microplate reader (Tecan, Mannedorf, Switzerland).

Nanoparticle feed suspensions were created by diluting the Fluosphere® stock suspensions (concentrations of about 3 × 10^{13} and 4 × 10^{15} particles/mL for the 100 and 20 nm particles, respectively) with 10 mM phosphate buffered saline (PBS) at pH 7.4. Feed concentrations of ~3 × 10^{10} particles/mL were used for the 100 nm particles and ~4 × 10^{12} particles/mL were used for the 20 nm particles to match typical concentrations of LV [5] and AAV [11] entering the final ultrafiltration step of the downstream process. The 100 nm nanoparticle feed was treated by ultrasonication (VWR International, Radnor, United States) for 15 min at a frequency of 35 kHz to ensure complete dispersion of the nanoparticles as suggested by the manufacturer [29]. DLS measurements revealed that the 20 nm nanoparticle feed remained stable without any evidence of significant particle aggregation over extended periods of time.

2.2. Single pass tangential flow filtration

SPTFF experiments were performed using Pellicon® 3 modules with 88 cm^2 of Ultracel® (composite regenerated cellulose) flat-sheet membranes (MilliporeSigma, Burlington, United States). To ensure that the membranes were fully retentive to the nanoparticles, membranes with 100 kDa and 300 kDa nominal molecular weight cutoffs were used during experiments with the 20 and 100 nm-sized particles, respectively. Cassettes were secured within a Pellicon® Mini TFF Cassette Holder (MilliporeSigma, Burlington, United States) and torqued to 190 inch-pounds to prevent leakage. Masterflex® pumps (Avantor, Radnor, United States) were placed on the feed inlet and retentate outlet lines to control the overall system conversion (φ), which is equal to the ratio of the permeate to feed flow rates.

The permeate channel contains two ports: port “P1” lies directly adjacent to the feed inlet, while port “P2” sits opposite the retentate outlet. Data were obtained using three different flow configurations by manipulating permeate collection through these ports, as shown schematically in Fig. 1.

The traditional operating configuration is shown in the left panel and is denoted as “convergent” permeate flow. Under these conditions P1 is closed, thereby directing all the collected permeate out through port P2. The “divergent” permeate flow configuration (middle panel) allows permeate collection through both permeate ports; a pump was placed on P1 to control the fraction of the total permeate flow collected through that port (with the flow rate through P2 controlled based on the setting of the retentate outlet pump). “Co-current” permeate flow (right panel) is generated by using a pump to feed clean buffer in through P1; this balances the axial pressure drop in the permeate and retentate channels as discussed by van Reis et al. [30].

Ashcroft® digital pressure gauges (Ashcroft, Stratford, United States) were placed on the feed, retentate, and permeate lines, with the pressure at P2 always kept at atmospheric. The mean transmembrane pressure (TMP) was evaluated as:

$$TMP = \frac{P_{f,in} + P_{r,out}}{2} - \frac{P_{p1} + P_{p2}}{2} \tag{1}$$

where $P_{f,in}$, $P_{r,o_{ut}}, P_{p1}$, and P_{p2} are the pressures at the feed inlet, retentate outlet, and the two permeate ports, respectively.

Flux-stepping experiments were performed to identify the critical flux for different operating conditions. These experiments were performed in full recirculation mode, in which the retentate and permeate streams exiting the module were recycled back to the feed vessel. The feed flow rate was kept constant, with the permeate flux increased stepwise every 40–60 min [31]. The nanoparticle concentration in the feed reservoir and the system TMP were monitored during each flux step to identify conditions that led to significant nanoparticle yield losses (>25 %) and/or significant membrane fouling (corresponding to a TMP gradient >0.03 kPa/min).

Experiments were also performed with two Pellicon® 3 cassettes in series, with both the feed and permeate channels of the two cassettes connected to simulate the behavior of a single 40 cm long cassette (illustrated in Fig. 2 for the convergent flow configuration). Note that commercial SPTFF modules commonly incorporate 3 or more cassettes in both series and parallel configurations. This two-in-series configuration made it possible to explore the variation in nanoparticle accumulation within the module as a function of position without the complexity of the series/parallel configurations used in commercial modules. At the end of each filtration, the flow was stopped, the two cassettes were disconnected, the permeate port(s) were clamped, and 50 mL of buffer (5.7 L/m^2 for each cassette) was then flushed separately through the individual retentate channels in two aliquots (first 30 mL followed by 20 mL). The number of nanoparticles accumulated within each filter was calculated from the volume and fluorescence intensity of the collected buffer flush.

3. Local wall concentration model

The Pellicon® 3 cassette has a retentate channel bounded by two semi-permeable membranes, creating a system with one retentate flow path and two (outer) permeate collection channels (see Fig. 1). All three channels contain mesh-like spacers (C-screens) that support the membranes while also providing increased mass transfer in the retentate.

The local pressure and flow variations in the z (axial) direction were evaluated by solving the system of 4 coupled ordinary differential equations [22]:

$$\frac{dP_r}{dz} = -\beta_r \mu Q_r \qquad \frac{dQ_r}{dz} = -2wJ \tag{2}$$

$$\frac{dP_p}{dz} = -\beta_p \mu Q_p \qquad \frac{dQ_p}{dz} = 2wJ \tag{3}$$

where P and Q are the local pressures and volumetric flow rates within the cassette, and the subscripts “r” and “p” denote the retentate and permeate channels, respectively. J is the local filtrate flux, μ is the solution viscosity, and w is the channel width. β_r and β_p are parameters that describe the parasitic pressure losses in the retentate and permeate channels, respectively. These were both evaluated experimentally by measuring the pressure drop as a function of flow rate using DI water at high feed (or permeate) flow rates in the absence of any net ultrafiltration.

The local filtrate flux was assumed to be proportional to the local

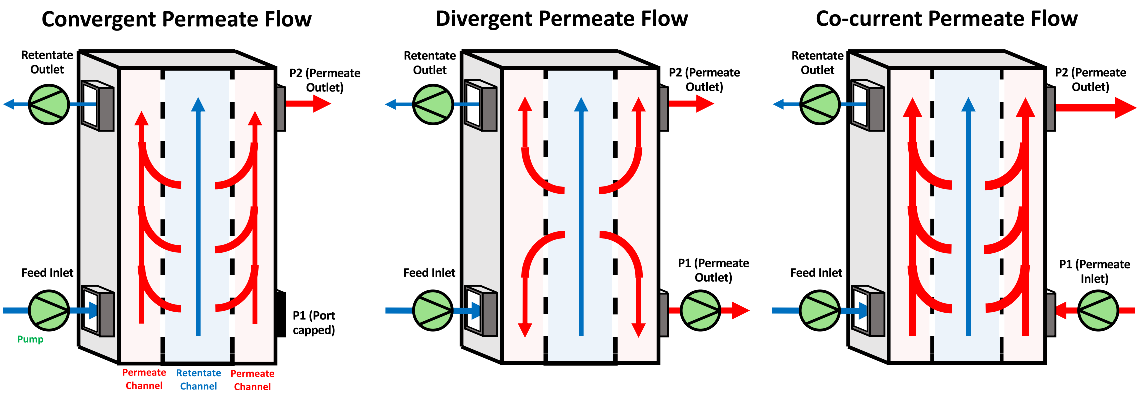

Fig. 1. Schematic diagram of permeate flow configurations. Retentate channel is shaded light blue while the permeate channels are shaded light red. Pumps are shown in green. (For interpretation of the references to colour in this figure legend, the reader is referred to the Web version of this article.)

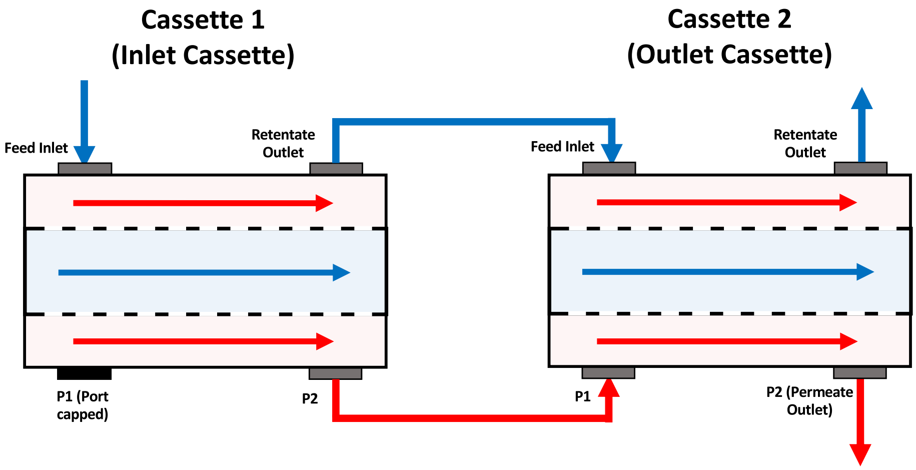

Fig. 2. Schematic diagram of two-in-series with convergent permeate flow SPTFF configuration. Retentate channel is shaded light blue while the permeate channels are shaded light red. (For interpretation of the references to colour in this figure legend, the reader is referred to the Web version of this article.)

transmembrane pressure difference:

$$J = L_p(P_r - P_p) \tag{4}$$

where L_p is the membrane permeability. Equation (4) neglects the effects of membrane fouling as well as any resistance provided by the nanoparticles that accumulate in the boundary layer adjacent to the membrane. This should be valid during operation below the critical flux (discussed in more detail subsequently). Equations (2) through (4) were solved simultaneously to evaluate the pressure and flux profiles as a function of z for any combination of the inlet TMP, feed flow rate, and conversion.

Typical results for the predicted retentate and permeate pressures in two linked Pellicon® 3 modules (total length of 40 cm) with 300 kDa membranes operated with convergent permeate flow are shown in Fig. 3 for $J_{feed} = 102$ L/m^2/h (LMH) at both 50 % and 90 % conversion. The permeate pressure at the system outlet (z = 0.40 m) was set to 0 kPa, with the inlet TMP then adjusted to give the desired conversion. Under these conditions, the pressure in the feed channel is always greater than that in the permeate, leading to a positive TMP and a positive filtrate flux across the entire length of the module. In both cases, the retentate pressure decreases most rapidly near the inlet of the device (where the retentate flow rate is highest) while the permeate pressure is relatively constant near the device inlet. At low conversion (φ = 50 %), the pressures in the retentate and permeate channels converge, leading to a monotonic decline in filtrate flux along the channel length. As the conversion is increased, the permeate pressure decreases more rapidly near the outlet due to an increase in the permeate flow rate in this region of the module. This effect leads to a local minimum in the filtrate flux (at z = 0.22 m) as seen in the lower panel of Fig. 3.

The local bulk nanoparticle concentration within the module can be determined directly from the local retentate flow rate as:

$$C_b(z) = C_b^{inlet}\left(\frac{Q_r^{inlet}}{Q_r}\right) \tag{5}$$

which is valid assuming complete nanoparticle retention and no nanoparticle accumulation within the module, i.e., the system is assumed to be operating at steady state with negligible nanoparticle accumulation in the concentration polarization boundary layer. The local concentration at the membrane surface (C_w) was then evaluated using the modified polarization equation presented by Chaubal and Zydney [18], which specifically accounts for the effects of the filtrate flux (transmembrane velocity) on particle transport to the membrane surface:

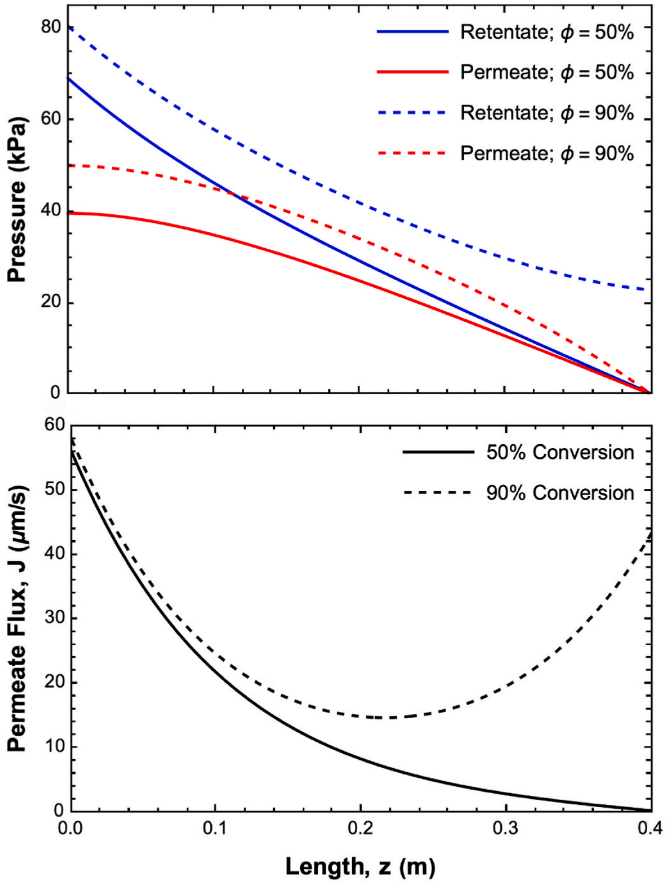

Fig. 3. Model predictions for the local retentate and permeate pressures (top panel) and local filtrate flux (bottom panel) for two connected Pellicon® 3 cassettes (total length of 0.4 m) operated with convergent permeate flow at a feed flux of 102 LMH (28.3 μm/s) at 50 % and 90 % conversion.

$$C_w(z) = C_b(z)\left(\frac{J}{k_o}\right)^3 \tag{6}$$

k_o is the local mass transfer coefficient within the membrane module, which was evaluated from the Sherwood number correlation for spacer-filled channels presented by Da Costa et al. [32]:

$$Sh = \frac{k_o\, d_h}{D} = 0.664\, Re^{0.5}\, Sc^{0.33} \left(\frac{d_h}{l_m}\right)^{0.5} \tag{7}$$

where the particle diffusivity (D), Schmidt Number $\left(Sc = \frac{\nu}{D}\right)$, channel hydraulic diameter (d_h), and spacer mesh length (l_m) are all assumed to be independent of axial position (z). The local Reynolds number is evaluated in terms of the local retentate flow rate:

$$Re = \frac{U\, d_h}{\nu} = \frac{Q_r\, d_h}{w\, h\, \nu} \tag{8}$$

with U the local crossflow velocity, ν the kinematic viscosity, and h the height of the retentate channel. The presence of the spacer within the retentate channel causes a significantly higher crossflow velocity than that seen in an open channel due to a reduction in the channel cross-sectional area. Thus, h was evaluated from the measured value of β_r based on the analytical expression for the pressure drop due to flow through an empty channel:

$$\beta_r = \frac{12}{h^3 w} \tag{9}$$

This gave $h = 96$ μm using $\beta_r = 6.3 \times 10^{14}$ m^{-4} as determined experimentally for the Pellicon® 3 module. Table 1 summarizes the physical parameters of the Pellicon® 3 cassettes with 300 kDa regenerated cellulose membranes that were used in the simulations.

The calculated wall concentration distribution for a feed containing 100 nm nanoparticles at an inlet concentration of $C_b^{inlet} = 3.5\,x\,10^{10}$ particles/mL with $J_{feed} = 102$ LMH at 50 %, 70 %, and 90 % conversion are shown in Fig. 4 using the same parameter values used in Fig. 3 (summarized in Table 1). The nanoparticle diffusion coefficient was evaluated using the Stokes-Einstein equation for a particle diameter of 122 nm (obtained from DLS as shown in Table S1) giving D = 4.0×10^{-12} m^2/s. At 50 % conversion, the wall concentration displays a maximum of 5 % by volume at the system inlet and then decreases over the entire channel length. As the conversion increases, $C_w(z)$ begins to increase over the latter portion of the channel, particularly when z > 0.25 m. This occurs due to the increasingly significant reduction in the local Reynolds number in combination with the increase in the bulk nanoparticle concentration at higher conversion. This effect leads to a maximum in the wall concentration at the channel exit, with $C_w{}^{max} = 8\%$ at 70 % conversion, and $C_w{}^{max} > 50\%$ at 90 % conversion. The very high C_w under these conditions will lead to membrane fouling near the channel exit, causing a reduction in the local filtrate flux. This is discussed in more detail in the context of the experimental results in the next section.

4. Results and discussion

4.1. Particle accumulation

The model calculations presented in the previous section clearly predict a significant variation in transmembrane pressure, filtrate flux, and nanoparticle concentration at the membrane surface with position along the length of the SPTFF module. In order to explore this behavior experimentally, SPTFF was performed using two connected Pellicon® 3 cassettes, referred to as a two-in-series configuration, with convergent permeate flow (illustrated in Fig. 2). Thus, the permeate inlet port in the first cassette was kept closed, while the permeate exiting the first cassette was fed directly into the permeate inlet of the second cassette. This configuration mimics the behavior of a 40 cm long module, with all filtrate collected from the downstream permeate exit port. The system was operated in total recycle mode for 90 min at a feed flux of 102 LMH (based on the total membrane area for the two cassettes) with $C_b^{inlet} = 3.5\,x\,10^{10}$ particles/mL. Separate experiments were performed at conversions of 50, 70, and 90 %. Following each experiment, the cassettes were decoupled, the permeate ports were closed, and 50 mL of buffer was flushed through the individual feed channels at 102 LMH (zero net ultrafiltration) to recover any nanoparticles that may have accumulated within each cassette. This typically restored >80 % of the original membrane permeability, suggesting that nanoparticle deposition is largely reversible. The individual cassettes were then cleaned by recirculating 0.3 N NaOH through the system for 45–60 min to further restore the membrane permeability between runs; all the data in Fig. 5 were obtained with the same two-in-series module to eliminate any effects of membrane-to-membrane variability.

Table 1
Physical properties of Pellicon® 3 cassettes with 300 kDa regenerated cellulose membranes.

Channel Length, L:	0.2 m (per channel)
Channel Width, w:	0.022 m
Retentate Channel Height, h:	9.6×10^{-5} m
Membrane Area (per cassette):	0.0088 m^2
Hydraulic Diameter, d_h:	3.3×10^{-4} m
Mesh Length, l_m:	3.5×10^{-4} m
Membrane Permeability, L_p:	1.9×10^{-9} m/Pa*s
Retentate Pressure Loss, β_r:	6.3×10^{14} m^{-4}
Permeate Pressure Loss, β_p:	5.8×10^{14} m^{-4}

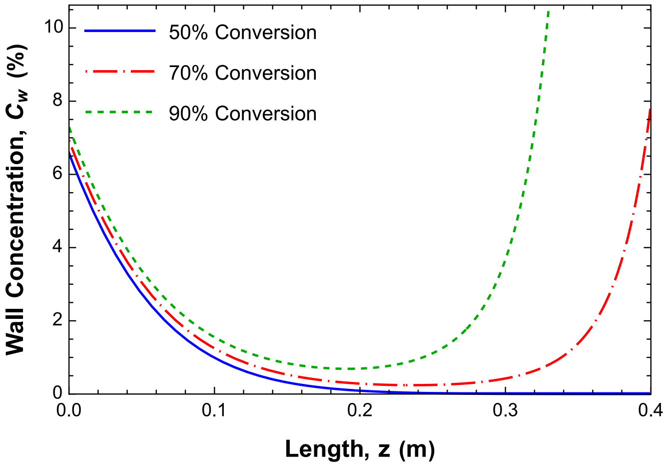

Fig. 4. Model simulations showing the variation of the wall concentration with axial position for two connected Pellicon® 3 cassettes operated with convergent permeate flow at a feed flux of 102 LMH and 50 %, 70 %, and 90 % conversion. Inlet nanoparticle concentration is $3.5\,x\,10^{10}$ particles/mL, corresponding to ~0.0018 % by volume.

The results from these experiments are shown in the top panel of Fig. 5 as the fraction of total nanoparticles recovered from both the first and second cassettes at the three different conversions. At a conversion of 50 %, more than 80 % of the nanoparticles are recovered in the first cassette. In contrast, approximately 75 % of the nanoparticles are recovered in the second cassette when the conversion is increased to 90 %. The results at 70 % conversion fall between these extremes, with relatively similar nanoparticle recovery across the two cassettes. These results are consistent with the simulated wall concentration distributions presented previously in Fig. 4, with an increase in conversion forcing the predicted wall concentration, as well as the observed nanoparticle accumulation, to increase towards the outlet of the long module.

The bottom panel of Fig. 5 shows model predictions for the fractional nanoparticle accumulation in each cassette. In this case, the extent of nanoparticle accumulation at any given location was calculated by estimating the mass of particles within the concentration boundary layer (m_{bl}) using the wall concentration profiles presented in Fig. 4. First, the thickness of the boundary layer was evaluated as $\delta = \frac{D}{k_o}$, with the local mass transfer coefficient calculated using Equation (7). Next, a linear

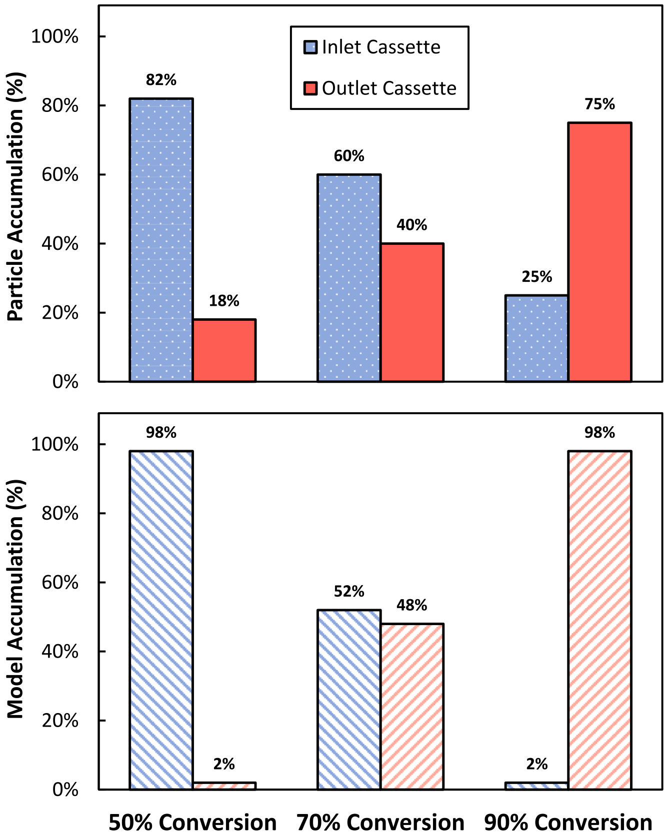

Fig. 5. Accumulation of 100 nm nanoparticles in the inlet and outlet cassettes at different conversions. Experiments were performed at a feed flux of 102 LMH and $C_b^{inlet} = 3.5\, x\, 10^{10}$ particles/mL for a two-in-series configuration with convergent permeate flow. Top panel shows experimental results while bottom panel shows model predictions.

concentration profile between the wall and the bulk concentration was assumed for the sake of mathematical simplicity. Thus, m_{bl} in each cassette was determined by integrating the average of C_w and C_b over the volume of the boundary layer:

$$m_{bl,1} = 2w \int_0^L \frac{C_b + C_w}{2}\, \delta\, dz \tag{10}$$

where L is the length of the first Pellicon® 3 cassette. A similar expression was used for the second cassette, but with the integration performed from z = L to z = 2L. The model predicts that 98 % of the nanoparticles will be recovered in the first cassette at 50 % conversion, with this value decreasing to only 2 % as the conversion increases to 90 %. The model predictions exhibit good qualitative agreement with the experimental results, although the model overpredicts the magnitude of the shift in nanoparticle accumulation towards the outlet with increasing conversion. This may well reflect some non-specific nanoparticle deposition that occurs at small values of C_w that is not accounted for in the model. Alternatively, this could be due to the inability to completely recover all the deposited nanoparticles in regions with very high local wall concentrations.

Similar results were obtained from experiments performed with 20 nm (AAV-sized) nanoparticles at a feed concentration of ~4 × 10^{12} particles/mL (0.01 % by volume) using Pellicon® 3 cassettes with 100 kDa Ultracel® membranes; the smaller MWCO was required to fully retain the 20 nm nanoparticles. The data again show a shift in nanoparticle accumulation towards the module outlet with increasing conversion. At 50 % conversion, 96 % of the AAV-sized nanoparticles were recovered from cassette 1, whereas at 90 % conversion 66 % of the nanoparticles were recovered from cassette 2 (see Supplemental Fig. S1). Model calculations were performed using the same framework as that used for the 100 nm nanoparticles, but with a larger diffusion coefficient for the 20 nm nanoparticles as evaluated using the Stokes-Einstein equation ($D = 1.29 \times 10^{-11}$ m^2/s). The model effectively captures the experimental observations by once again predicting the shift in nanoparticle accumulation with increasing conversion. The good agreement between the model and data for both the 20 and 100 nm nanoparticles suggests that this general framework should be applicable across multiple viral vector modalities.

The axial variation in the accumulation of 100 nm nanoparticles for the two-in-series module was also examined for different permeate flow configurations. In each case, the system was operated at a feed flux of 102 LMH with 70 % overall conversion. The data with convergent permeate flow were taken from Fig. 5. The co-current flow configuration used the same connections between the cassettes, but additional permeate was pumped into P1 of the first cassette at a flow rate of 7.9 mL/min (compared to the feed flow rate of 30 mL/min). This generated a transmembrane pressure drop of 17 kPa (2.5 psi) at the inlet to the first cassette and 16 kPa (2.4 psi) at the exit of the second cassette. The divergent flow configuration used a pump to collect 34 LMH (47.6 %) of the permeate from P1 of cassette 1, with the remainder of the permeate collected from P2 of cassette 2; the outlet permeate port from cassette 1 was connected to the inlet permeate port of cassette 2. The majority of the nanoparticle accumulation in the co-current flow configuration occurred in the second cassette, consistent with the greater bulk nanoparticle concentration and lower Reynolds number at the system outlet; the permeate flux should be relatively similar in both cassettes based on the similar values of the TMP. In contrast, 93 % of the nanoparticle accumulation occurred in the first cassette with the divergent flow configuration due to the higher permeate flux in this cassette; the TMP at the inlet of cassette 1 was 32 kPa (4.7 psi) compared to only 2.1 kPa (0.3 psi) at the outlet of cassette 2. The convergent flow configuration has an intermediate behavior, with relatively uniform nanoparticle accumulation in the two cassettes.

The bottom panel of Fig. 6 shows model predictions for the different flow configurations, again determined based on the average values of the wall concentration in the two cassettes as determined from Equation (10), with $C_w(z)$ evaluated using Equation (6). The model accurately predicts the differences in nanoparticle accumulation for the three different flow configurations. The quantitative agreement between the model and data is excellent given the relatively simple description used for the flow and nanoparticle transport. The model predicts 13 % accumulation of nanoparticles in the first cassette with the co-current configuration compared to the 22 % observed experimentally. This increased to 52 % and then 95 % for the convergent and divergent configurations compared to the experimental values of 60 % and 93 %. These results clearly demonstrate that one can shift the location of nanoparticle accumulation in a long SPTFF module based on both the conversion and permeate flow control strategy, and that the local C_w model can accurately describe the physical phenomena controlling this behavior. A full compilation of all trials performed, along with a summary of the model predictions, is provided in Table 2.

In order to mitigate particle accumulation during SPTFF at higher conversion, a divergent permeate flow was implemented to reduce the local pressure drop at the system outlet. One of the advantages of using the divergent flow configuration is that the transmembrane pressure and flow distributions within the SPTFF module can be fine-tuned by controlling the fraction of filtrate that is collected from the permeate inlet port (P1). A series of experiments were again performed using the two-in-series system with connected permeate channels (to mimic a 40 cm long cassette). The system was operated at $J_{feed} = 55$ LMH and 80 % conversion, but the fraction of permeate collected from the first port (f_p) was varied between 0 % and 100 %. The extent of yield loss due to boundary layer accumulation during an SPTFF process was assessed experimentally by operating the system in total recycle mode while monitoring nanoparticle depletion in the feed reservoir over time. It is

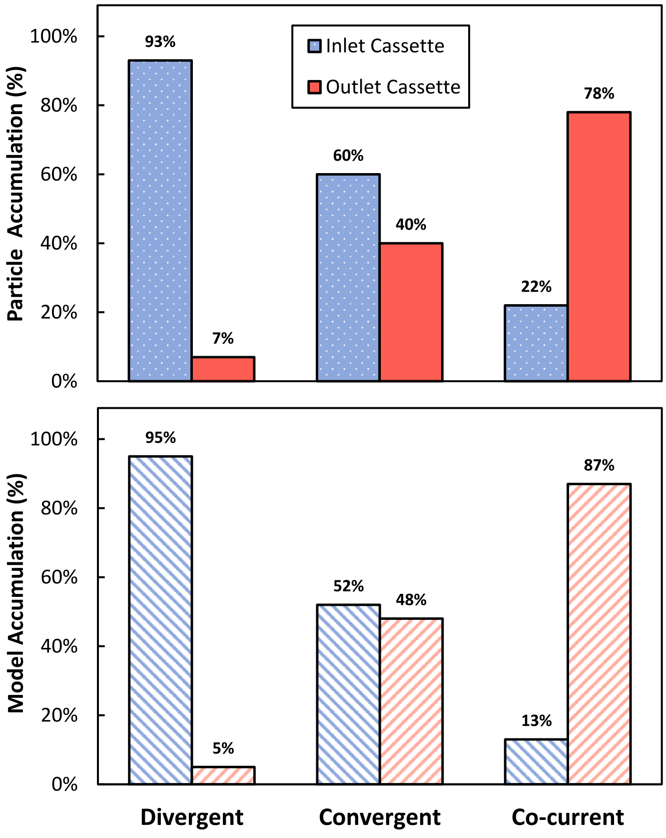

Fig. 6. Accumulation of 100 nm nanoparticles in the inlet and outlet cassettes for different permeate flow configurations. Experiments were performed at a feed flux of 102 LMH at 70 % conversion and $C_b^{inlet} = 3.5\,x\,10^{10}$ particles/mL with a two-in-series module. Top panel shows experimental results while bottom panel shows model calculations. The definitions of the different flow configurations are provided in the text.

worth noting that “nanoparticle depletion” will depend on both the mass loading of nanoparticles and any dilution effects associated with the hold-up volume within the membrane module and tubing. Therefore, each experiment was performed using 500 mL of feed material at a concentration of 3×10^{10} particles/mL (constant mass loading of 8.5×10^{14} particles/m^2 membrane area). The dilution effects were also standardized by operating each experiment with the same SPTFF module/tubing assembly (giving approximately 15 mL hold up volume). As shown in the top panel of Fig. 7, approximately 65 % of the nanoparticles were deposited within the two-in-series system after 60 min of operation when all the permeate was taken out of the inlet permeate port (i.e., at $f_p = 1.0$). This decreased to <40 % at $f_p = 0.3$ before then increasing to 47 % when all the permeate was collected through the permeate port near the filter exit (i.e., with the inlet permeate port clamped shut, which is identical to the convergent flow configuration). In addition, the fraction of nanoparticles recovered from the first cassette (at the completion of the run) went from 23 % when $f_p = 0$ to 97 % when $f_p = 1$.

The solid curve in the bottom panel of Fig. 7 shows the model predictions, developed by dividing the calculated number of nanoparticles that accumulated within the boundary layer by the total number of nanoparticles in the feed. The high degree of nanoparticle loss as $f_p \rightarrow 0$ is due to the high wall concentration near the exit of the cassette, which is the region where the bulk nanoparticle concentration is highest and the retentate flow rate (and thus the mass transfer coefficient) are the smallest. The behavior as $f_p \rightarrow 1$ is very different, with the majority of the nanoparticle loss occurring near the inlet of the cassette due to the high permeate flux associated with the large inlet TMP. The model predicts a minimum in nanoparticle loss at $f_p = 0.41$, which is in good agreement with the experimental results. It is important to note that the calculated values of m_{bl} are significantly smaller than the experimental nanoparticle loss, suggesting that there is substantial nanoparticle deposition due to cake formation and/or nanoparticle adsorption within the retentate channel. The model is also able to predict the change in location of nanoparticle accumulation, with the predicted fraction of nanoparticles that were accumulated in the first cassette increasing from

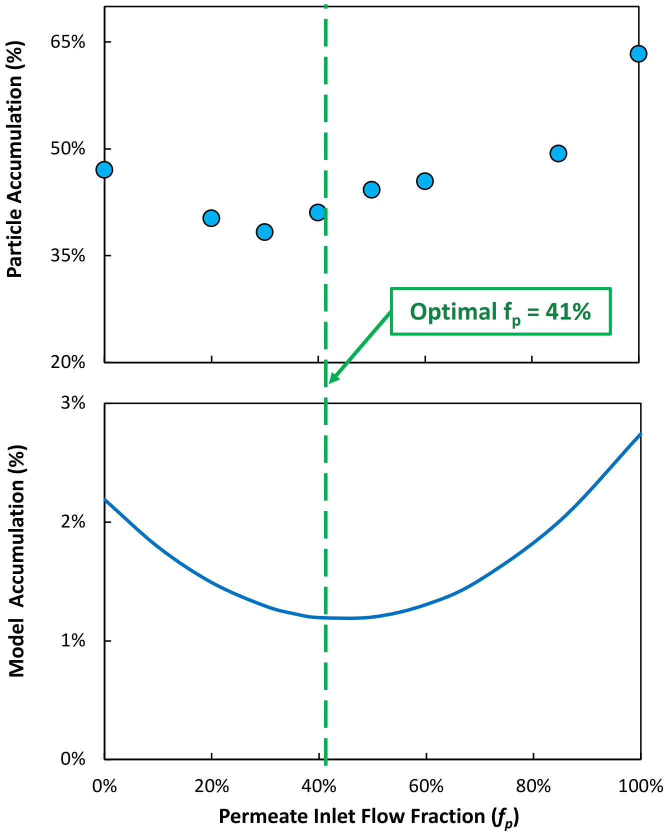

Fig. 7. Overall particle accumulation within a two-in-series module operated at a feed flux of 55 LMH and 80 % conversion with $C_b^{inlet} = 3\,x\,10^{10}$ particles/mL as a function of the fraction of the permeate collected through the inlet permeate port. Top panel: Experimental results obtained after 60 min operation. Bottom panel: Model calculations.

Table 2
Summary of model predictions and experimental results for particle accumulation in the two-in-series Pellicon® 3 module with 300 kDa regenerated cellulose membranes at a feed flux of 102 LMH. Data were collected at varied permeate conversions and flow configurations.

Conversion	Volume Concentration Factor (VCF)	Configuration	Flux at P1 (LMH)	Inlet Accumulation (%)	Model Inlet Accumulation (%)
50 %	2.0	Convergent	0 LMH	82 %	98 %
70 %	3.3	Convergent	0 LMH	60 %	52 %
90 %	10.0	Convergent	0 LMH	25 %	2 %
70 %	3.3	Divergent	34 LMH out	93 %	95 %
70 %	3.3	Co-current	27 LMH in	22 %	13 %

14.1 % at $f_p = 0$ to 95.5 % as $f_p \rightarrow 1$ (data not presented).

4.2. *Critical flux*

Previous studies have shown that sustainable SPTFF operation with minimal particle loss and membrane fouling can be achieved by operating the system below a critical value of the permeate flux [33,34]. The presence of a critical flux was explored using a modified flux stepping procedure as described in the *Materials and Methods*, with results for a single Pellicon® 3 cassette operated with convergent permeate flow at $J_{feed} = 102$ LMH shown in Fig. 8. The experiment began with the permeate flux set at 48 LMH giving a conversion of 47 %. The permeate flux was maintained at that value for 50 min, at which point the permeate line was clamped and the feed recirculated through the cassette for approximately 5 min (at zero net ultrafiltration) to re-suspend the majority of nanoparticles that were deposited on the membrane surface during the ultrafiltration. This process was repeated using permeate fluxes of 61, 68, and 75 LMH with a 5 min period at zero net ultrafiltration between each flux.

Fig. 8 shows results for both the nanoparticle concentration in the feed reservoir (blue diamonds) and the mean transmembrane pressure (red circles) as a function of time during this modified flux-stepping experiment. The nanoparticle concentration at a flux of 48 LMH (corresponding to 47 % conversion) decreased by 11 % over the 60 min filtration, with the TMP remaining nearly constant. There was then a small increase in the nanoparticle concentration after the 5 min recirculation period, although the nanoparticle concentration at the start of the second cycle remained about 8 % smaller than that at the start of the experiment, likely due to a combination of hold-up volume/dilution effects along with any "irreversible" nanoparticle loss. The results during the second cycle at a flux of 61 LMH (60 % conversion) were similar, with a slightly larger drop in the nanoparticle concentration but a stable TMP. However, when the permeate flux was increased to 68 LMH (67 % conversion), the nanoparticle concentration in the reservoir declined by more than 33 % over the 50 min filtration due to the significant accumulation of nanoparticles within the concentration polarization boundary layer. We defined this "boundary layer" critical flux, J_{bl}, as the flux at which the nanoparticle concentration first declined by at least 25 % within 50 min. A further increase in the permeate flux to 75 LMH (73 % conversion) caused an even larger drop in the nanoparticle concentration, with the TMP now increasing by more than 1.4 kPa (0.2 psi) over the 50 min cycle, corresponding to a TMP gradient of 0.034 kPa/min. This large increase in TMP was used to define the "fouling" critical flux, J_{foul}, as the filtrate flux at which the TMP gradient first exceeds 0.03 kPa/min. The critical flux was taken as the average of the permeate fluxes just above and below the transition point(s). This yielded a J_{bl} of 65 LMH, and a J_{foul} of 71 LMH under these conditions. In all the experiments performed in this study, nanoparticle depletion always preceded membrane fouling, i.e., J_{bl} was always less than J_{foul}; this suggests that particle depletion is an appropriate indicator for sustainable SPTFF performance.

The effects of the inlet nanoparticle concentration on the critical conversion (defined as the ratio of J_{foul} to J_{feed}) for a single Pellicon® 3 cassette operated with convergent permeate flow are shown in Fig. 9. Flux-stepping experiments were performed at a feed flux of 102 LMH for

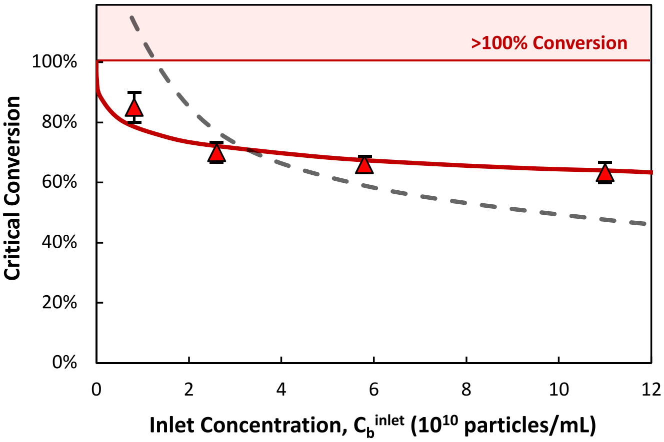

Fig. 9. Effect of inlet nanoparticle concentration on the critical conversion (evaluated based on the measured value of J_{foul}) for a single Pellicon® 3 cassette operated with convergent permeate flow at a feed flux of 102 L/m^2/h. Solid and dashed curves are model calculations developed using the local and average concentration polarization models, respectively.

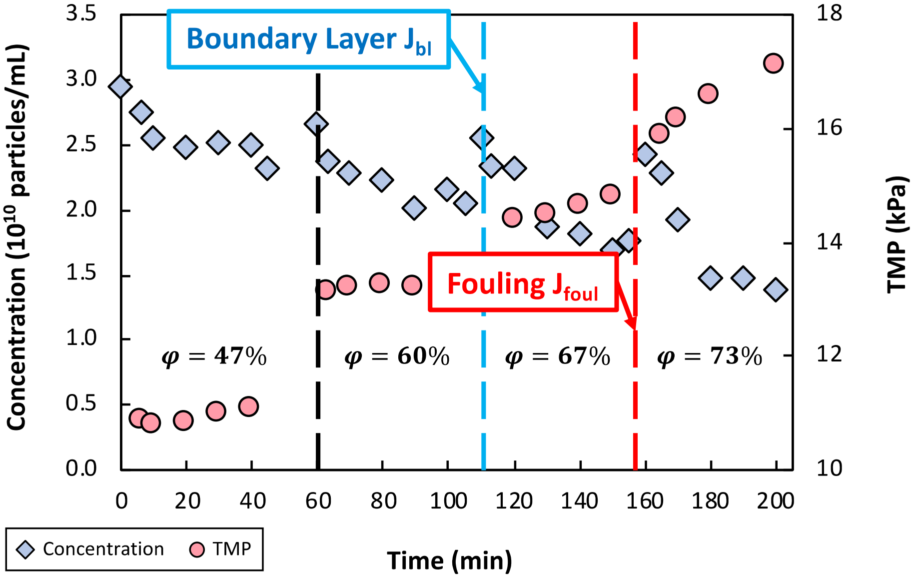

Fig. 8. Bulk nanoparticle concentration (blue diamonds) and transmembrane pressure (red circles) during a flux stepping experiment performed with a single Pellicon® 3 cassette with convergent permeate flow at a feed flux of 102 LMH using permeate fluxes of 48, 61, 68, and 75 L/m^2/h (corresponding to conversions of 47, 60, 67, and 73 %). Conversion values are provided on the plot. (For interpretation of the references to colour in this figure legend, the reader is referred to the Web version of this article.)

four separate inlet nanoparticle concentrations, using a fresh Pellicon® 3 cassette for each experiment. In each case, the critical conversion was evaluated based on the value of the fouling critical flux. The error bars represent the range of flux values tested just below and just above J_{foul}. The critical conversion was 85 % for the experiment with $C_b^{inlet} = 8 \times 10^9$ nanoparticles/mL, corresponding to a volume concentration factor (VCF) of 6.7, but this decreased to a conversion of only 64 % (VCF = 2.8) when C_b^{inlet} increased to 1.1×10^{11} particles/mL.

The solid and dashed curves in Fig. 9 are model calculations developed by assuming that the critical flux occurs when the nanoparticle concentration at the membrane surface (C_w) exceeds some maximum value. The dashed curve is the model developed previously by Chaubal and Zydney [18], which assumes that k_o, J_v, and C_b (and therefore C_w) are all independent of axial position, with their values determined based on the inlet conditions. The best fit for this model was obtained using a critical $C_w = 8.3$ % by volume. Although this simple averaged C_w model predicts the observed decrease in the critical conversion with increasing nanoparticle concentration, the slope is much steeper than that seen in the experiments. In addition, the predicted conversion at $C_b^{inlet} < 10^{10}$ particles/mL is greater than 100 % since the inlet feed flow rate (and thus the Reynolds number) remains positive even when the retentate flow rate at the channel exit becomes negative. The solid curve is based on the local concentration polarization model developed in this manuscript, which assumes that fouling occurs when the local wall concentration at any point within the channel exceeds 15 % by volume. This value of the critical wall concentration was determined by fitting the model to the data by eye. At a wall concentration of 15 %, the nanoparticle deposit likely provides a sufficient resistance to flow to cause the TMP to increase significantly during the constant flux filtration. The model is in very good agreement with the experimental results, properly capturing the reduction in critical conversion with increasing inlet nanoparticle concentration, with the maximum conversion approaching 100 % only as C_b^{inlet} approaches zero.

The critical conversion is also a function of the feed flux as shown in Fig. 10 for data obtained at an inlet nanoparticle concentration of 2.5×10^{11} particles/mL using convergent permeate flow. Although increasing the feed flux causes an increase in J_{foul}, the dependence is much less than linear primarily due to the 0.5 power dependence of the mass transfer coefficient on the local Reynolds number. The net result is that the critical conversion decreases from >95 % (VCF >20) at a feed flux of 14 LMH to less than 50 % (VCF <2) at a feed flux of 410 LMH. The solid red curve is again the model calculation for the local concentration polarization model, using the same value of the local critical wall concentration of 15 %. The model predicts a rapid decrease in the critical conversion at low feed flux followed by a plateau and then another rapid decrease at feed fluxes above 360 LMH. This unusual behavior arises from a shift in the location of the maximum wall concentration. At low feed flux (high critical conversion), the transmembrane pressure is relatively uniform along the length of the module, with the maximum value of C_w occurring at the exit of the filter due to the low flow rate and high bulk nanoparticle concentration at that location. As the feed flux increases, the pressure drop due to flow through the retentate channel also increases, leading to a large gradient in the local transmembrane pressure. Under these conditions, the maximum wall concentration occurs at the channel inlet since that is where the TMP and local permeate flux are greatest. The transition between the maximum wall concentration at the channel outlet and inlet occurs at $J_{feed} = 360$ LMH, giving rise to the observed inflection point in the model calculations. This behavior is completely absent in the average C_w model (dashed curve), which also predicts a conversion >100 % for feed fluxes less than 63 LMH.

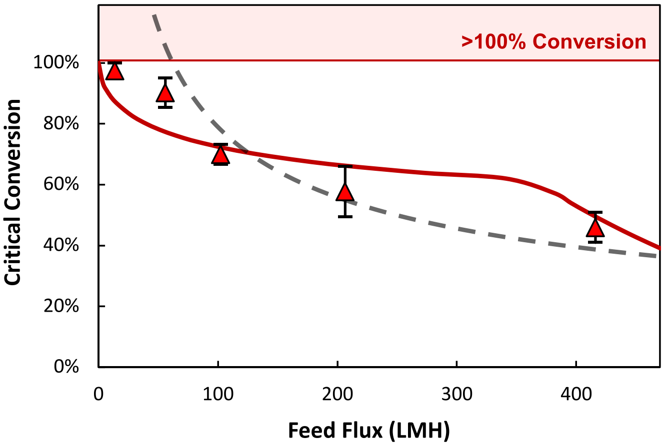

Fig. 10. Effect of feed flux on the critical conversion (evaluated based on the measured value of J_{foul}) for a single Pellicon® 3 cassette operated with convergent permeate flow at an inlet nanoparticle concentration around 2.5×10^{10} particles/mL.

5. Conclusions

Single pass tangential flow filtration is increasingly used in the downstream processing of monoclonal antibodies, providing opportunities for process intensification and greater manufacturing productivity. SPTFF can also have a major impact in the production of viral vectors in which the lower flow rates and single pass operation could lead to significant improvements in product quality. This study examined the effects of the flow and pressure distributions on SPTFF performance using a model nanoparticle system, combining detailed experimental measurements with a new concentration polarization modeling framework that was used to predict the variation in the local wall concentration along the length of the membrane. The use of fluorescent nanoparticles allowed for simple recovery of nanoparticles deposited within the module, with the total number of nanoparticles evaluated quantitatively using fluorescence intensity.

Experiments performed with two Pellicon® 3 cassettes in series showed that the location of nanoparticle accumulation shifts based on both the conversion and the permeate flow configuration. At low conversion, nanoparticles deposit preferentially near the module inlet due to the high local transmembrane pressure in this region. The behavior is very different at high conversion where the low retentate flow rate and high bulk nanoparticle concentration lead to preferential nanoparticle deposition near the module outlet. These results are in very good agreement with the predicted variation in C_w and the estimated nanoparticle accumulation within the boundary layer. It is important to note that the model involves no fitted parameters; the module geometry and pressure loss parameters were all evaluated from independent experimental measurements performed with buffer (i.e., in the complete absence of any nanoparticles).

The pressure profiles in the permeate flow channel within the Pellicon® 3 cassettes also have a significant impact on SPTFF performance, which was demonstrated by performing experiments with co-current, convergent, and divergent permeate flow configurations. At moderate conversion (e.g., $\varphi = 70\%$) nanoparticle deposition was relatively uniform with convergent permeate flow but was shifted towards the inlet with divergent flow and towards the outlet with co-current flow – these results were in good agreement with model predictions. At $J_{feed} = 55$ LMH and higher conversion ($\varphi = 80\%$), both the model and data show that particle accumulation within the boundary layer can be minimized using divergent flow – more specifically when 41 % of the total permeate flow is collected through the permeate inlet port. The model was also able to accurately describe the dependence of the fouling critical flux on the feed flux and inlet nanoparticle concentration based on the assumption that fouling occurs when the nanoparticle concentration at any point along the membrane surface (C_w) exceeds a critical value, which was found to be approximately 15 % by volume.

The opportunity to control SPTFF performance through the pressure profiles in both the permeate and retentate channels opens up new opportunities for the design and optimization of SPTFF modules for inline concentration of viral vectors. This includes the development of novel staged configurations in which the number of parallel flow channels is used to optimize the flow and pressure gradients. Future studies will be focused on demonstrating the applicability of this theoretical framework for SPTFF of different viral vector modalities, including both lentivirus and adeno-associated virus (AAV) that are of growing interest in gene therapy applications. This will include analysis of LV and AAV aggregation and shear sensitivity, both of which can affect the quality of the product generated by SPTFF.

Data availability

Data will be made available upon request.

CRediT authorship contribution statement

Akshay S. Chaubal: Writing – original draft, Investigation, Formal analysis, Data curation, Conceptualization. **Alexis J. Single:** Writing – review & editing, Investigation, Data curation. **Andrew L. Zydney:** Writing – review & editing, Supervision, Methodology, Funding acquisition, Conceptualization.

Declaration of competing interest

The authors declare that they have no known competing financial interests or personal relationships that could have appeared to influence the work reported in this paper.

Data availability

Data will be made available on request.

Acknowledgments

The authors would like to acknowledge Joe Hersey at MilliporeSigma for supplying the membranes used throughout this study. The authors would also like to thank Nicholas Marchand at Cytiva Life Sciences for his guidance and suggestions. Support for this work was provided through the Membrane Applications Science and Technology (MAST) Center, which is funded by grant numbers 1841474 and 2310832 from the NSF IUCRC program.

Appendix B. Supplementary data

Supplementary data to this article can be found online at https://doi.org/10.1016/j.memsci.2024.123276.

References

[1] Z. Zhao, A.C. Anselmo, S. Mitragotri, Viral vector-based gene therapies in the clinic, Bioeng Transl Med 7 (1) (2022) e10258, https://doi.org/10.1002/btm2.10258.

[2] Available online, https://www.fda.gov/vaccines-blood-biologics/cellular-gene-therapy-products/approved-cellular-and-gene-therapy-products. (Accessed 25 June 2023).

[3] Available online, https://www.fda.gov/vaccines-blood-biologics/cellular-gene-therapy-products/lenmeldy. (Accessed 25 June 2023).

[4] Available online, https://www.fda.gov/vaccines-blood-biologics/cellular-gene-therapy-products/beqvez. (Accessed 25 June 2023).

[5] C. Perry, A.C. Rayat, Lentiviral vector bioprocessing, Viruses 13 (2) (2021) 268, https://doi.org/10.3390/v13020268.

[6] M. Hebben, Downstream bioprocessing of AAV vectors: industrial challenges & regulatory requirements, Cell and Gene Therapy Insights 4 (2) (2018) 131–146, https://doi.org/10.18609/cgti.2018.016.

[7] S.R. Wickramasinghe, B. Kalbfuß, A. Zimmermann, V. Thom, U. Reichl, Tangential flow microfiltration and ultrafiltration for human influenza A virus concentration and purification, Biotechnol. Bioeng. 92 (2005) 199–208.

[8] R. van Reis, A. Zydney, Bioprocess membrane technology, J. Membr. Sci. 297 (1–2) (2007) 16–50, https://doi.org/10.1016/j.memsci.2007.02.045.

[9] D.J. Callahan, B. Stanley, Y. Li, Control of protein particle formation during ultrafiltration/diafiltration through interfacial protection, J. Pharmaceut. Sci. 103 (3) (2014) 862–869, https://doi.org/10.1002/jps.23861.

[10] A.J. Valkama, I. Oruetxebarria, E.M. Lipponen, H.M. Leinonen, P. Käyhty, H. Hynynen, V. Turkki, J. Malinen, T. Miinalainen, N. Heikura, N.R. Parker, S. Ylä-Herttuala, H.P. Lesch, Development of large-scale downstream processing for lentiviral vectors, Molecular Therapy - Methods & Clinical Development 17 (2020) 717–730, https://doi.org/10.1016/j.omtm.2020.03.025.

[11] A. Arunkumar, N. Singh, Ultrafiltration behavior of recombinant adeno-associated viral vectors used in gene therapy, J. Membr. Sci. 620 (2021) 118812, https://doi.org/10.1016/j.memsci.2020.118812.

[12] C. Casey, T. Gallos, Y. Alekseev, E. Ayturk, S. Pearl, Protein concentration with single-pass tangential flow filtration (SPTFF), J. Membr. Sci. 384 (1–2) (2011) 82–88, https://doi.org/10.1016/j.memsci.2011.09.004.

[13] C.J. Yehl, A.L. Zydney, Single-use single-pass tangential flow filtration using low-cost hollow fiber modules, J. Membr. Sci. 595 (2020) 117517.

[14] E. Madsen, J. Kaiser, U. Krühne, M. Pinelo, Single pass tangential flow filtration: critical operational variables, fouling, and main current applications, Sep. Purif. Technol. 291 (2022) 120949, https://doi.org/10.1016/j.seppur.2022.120949.

[15] A. Arunkumar, N. Singh, M. Peck, M.C. Borys, Z.J. Li, Investigation of single-pass tangential flow filtration (SPTFF) as an inline concentration step for cell culture harvest, J. Membr. Sci. 524 (2017) 20–32.

[16] S.B. Rahane, A. Gupta, P. Szymanski, D. Kinzlmaier, P. McGee, E. Goodrich, Concentration of clarified pool by single-pass tangential flow filtration to improve productivity of protein A capture step: impact of clarification strategies, Biotechnol. Bioeng. 121 (3) (2024) 1090–1101, https://doi.org/10.1002/bit.28634.

[17] R.M. Tona, R. Shah, K. Middaugh, J. Steve, J. Marques, B.R. Roszell, C. Jung, Process intensification for lentiviral vector manufacturing using tangential flow depth filtration, Molecular Therapy - Methods & Clinical Development 29 (2023) 93–107, https://doi.org/10.1016/j.omtm.2023.02.017.

[18] A.S. Chaubal, A.L. Zydney, Single-pass tangential flow filtration (SPTFF) of nanoparticles: achieving sustainable operation with dilute colloidal suspensions for gene therapy applications, Membranes 13 (2023) 433, https://doi.org/10.3390/membranes13040433.

[19] M.J. Huter, C. Jensch, J. Strube, Model validation and process design of continuous Single Pass Tangential Flow Filtration focusing on continuous bioprocessing for high protein concentrations, Processes 7 (2019) 781, https://doi.org/10.3390/pr7110781.

[20] G. Thakur, A.S. Rathore, Modelling and optimization of single-pass tangential flow ultrafiltration for continuous manufacturing of monoclonal antibodies, Sep. Purif. Technol. 276 (2021) 119341, https://doi.org/10.1016/j.seppur.2021.119341.

[21] M. Krippl, T. Kargl, M. Duerkop, A. Dürauer, Hybrid modeling reduces experimental effort to predict performance of serial and parallel single-pass tangential flow filtration, Sep. Purif. Technol. 276 (2021) 119277, https://doi.org/10.1016/j.seppur.2021.119277.

[22] M.G. Jabra, A.M. Lipinski, A.L. Zydney, Single pass tangential flow filtration (SPTFF) of monoclonal antibodies: experimental studies and theoretical analysis, J. Membr. Sci. 637 (2021) 119606.

[23] M.G. Jabra, A.L. Zydney, Design and optimization of single pass tangential flow filtration for inline concentration of monoclonal antibodies, J. Membr. Sci. 643 (2022) 120047, https://doi.org/10.1016/j.memsci.2021.120047.

[24] M. Pazouki, A.N. Wilton, D.R. Latulippe, An experimental study on sterile filtration of fluorescently labeled nanoparticles—the importance of surfactant concentration, Sep. Purif. Technol. 218 (2019) 217–226, https://doi.org/10.1016/j.seppur.2019.02.038.

[25] N. Taylor, W. Ma, A. Kristopeit, S. Wang, A.L. Zydney, Evaluation of a sterile filtration process for viral vaccines using a model nanoparticle suspension, Biotechnol. Bioeng. 118 (2020) 106–115.

[26] L.K. Chu, S.R. Wickramasinghe, X. Qian, A.L. Zydney, Retention and fouling during nanoparticle filtration: implications for membrane purification of biotherapeutics, Membranes 12 (2022) 299.

[27] M. Leach, et al., Role of microfiltration membrane morphology on nanoparticle purification to enhance downstream purification of viral vectors, ACS Appl. Bio Mater. 7 (2024) 3932–3941, https://doi.org/10.1021/acsabm.4c00272.

[28] L. Pang, K. Farkas, G. Bennett, A. Varsani, R. Easingwood, R. Tilley, U. Nowostawska, S. Lin, Mimicking filtration and transport of rotavirus and adenovirus in sand media using DNA-labeled protein-coated silica nanoparticles, Water Res. 62 (2014) 167–179, https://doi.org/10.1016/j.watres.2014.05.055.

[29] Molecular Probes Invitrogen Detection Technologies, Fluospheres Flourescent Microspheres, 2005 [Online] Available at: https://tools.thermofisher.com/content/sfs/manuals/mp05000.pdf.

[30] R. van Reis, S. Gadam, L.N. Frautschy, S. Orlando, E.M. Goodrich, S. Saksena, R. Kuriyel, C.M. Simpson, S. Pearl, A.L. Zydney, High performance tangential flow filtration, Biotechnol. Bioeng. 56 (1997) 71–82, https://doi.org/10.1002/(SICI)1097-0290(19971005)56:1<71::AID-BIT8>3.0.CO;2-S.

[31] M. Minervini, A.L. Zydney, Effect of module geometry on the sustainable flux during microfiltration of precipitated IgG, J. Membr. Sci. 660 (2022) 120834, https://doi.org/10.1016/j.memsci.2022.120834.

[32] A.R. Da Costa, A.G. Fane, D.E. Wiley, Spacer characterization and pressure drop modelling in spacer-filled channels for ultrafiltration, J. Membr. Sci. 87 (1994) 79–98, https://doi.org/10.1016/0376-7388(93)E0076-P.

[33] P. Bacchin, P. Aimar, R.W. Field, Critical and sustainable fluxes: theory, experiments and applications, J. Membr. Sci. 281 (1–2) (2006) 42–69, https://doi.org/10.1016/j.memsci.2006.04.014.

[34] M. Minervini, A. Behboudi, J.R. Marzella, A.L. Zydney, Optimizing particle morphology during antibody precipitation for enhanced tangential flow filtration performance, Sep. Purif. Technol. 338 (2024) 126574, https://doi.org/10.1016/j.seppur.2024.126574.